Rabi spectroscopy and excitation inhomogeneity in a one-dimensional optical lattice clock

S. Blatt,* J. W. Thomsen,† G. K. Campbell, A. D. Ludlow,‡ M. D. Swallows, M. J. Martin, M. M. Boyd,§ and J. Ye
JILA, National Institute of Standards and Technology and University of Colorado,
Department of Physics, University of Colorado, Boulder, Colorado 80309-0440, USA
(Received 8 June 2009; published 6 November 2009)

We investigate the influence of atomic motion on precision Rabi spectroscopy of ultracold fermionic atoms confined in a deep one-dimensional optical lattice. We analyze the spectral components of longitudinal sideband spectra and present a model to extract information about the transverse motion and sample temperature from their structure. Rabi spectroscopy of the clock transition itself is also influenced by atomic motion in the weakly confined transverse directions of the optical lattice. By deriving Rabi flopping and Rabi line shapes of the carrier transition, we obtain a model to quantify trap-state-dependent excitation inhomogeneities. The inhomogeneously excited ultracold fermions become distinguishable, which allows *s*-wave collisions. We derive a detailed model of this process and explain observed density shift data in terms of a dynamic mean-field shift of the clock transition.

DOI: 10.1103/PhysRevA.80.052703 PACS number(s): 37.10.Jk, 42.50.Md, 42.62.Eh, 34.50.Cx

I. INTRODUCTION

Evaluations of optical frequency standards based on ultracold neutral ^{87}Sr atoms confined in one-dimensional (1D) optical lattices now surpass [1,2] the best ^{133}Cs primary standards [3–5]. The high precision achieved with the Sr optical lattice clock relies on high quality factor optical spectroscopy [6] enabled by confining the atoms in a magic wavelength optical lattice [7] and probing along the strong confinement axis in the Lamb-Dicke and resolved sideband regimes [8,9]. No studies yet indicate a fundamental limit at the 10^{-17} level of accuracy [1,10–12]. Reaching new levels of accuracy demands that ever more subtle spectroscopic effects are taken into account. Recently, a density related clock frequency shift was measured [10], even though the clock is based on fermionic ^{87}Sr where collisions at temperatures of a few μK are suppressed by the Pauli exclusion principle.

In this paper, we present a systematic experimental and theoretical investigation of the Rabi spectroscopy process used in the ^{87}Sr optical lattice clock. This investigation results in a more detailed model of the density-dependent clock frequency shift. These results are used to describe our recent experimental work [10], which has led to several different theoretical models of fermion clock frequency shifts [13,14].

The experimental setup is described in Sec. II. We present a perturbative model of the 1D lattice in Sec. III, derive sideband spectra in Sec. IV, and show how temperature can be obtained from their shape. Furthermore, we discuss time-dependent Rabi flopping and spectroscopic line shapes as well as their dependence on sample temperature and probe-induced inhomogeneities in Sec. V. In particular, we identify the effect of transverse motion on the excitation process as the main source of inhomogeneity in the system causing atoms to lose their indistinguishability. Accurate modeling of the process in Sec. VI allows relating this loss of indistinguishability to a dynamic clock frequency shift proportional to the atomic density.

II. EXPERIMENTAL SETUP

The ultracold atomic sample of ^{87}Sr is produced by standard laser cooling techniques and trapped at the antinodes of a vertically oriented 1D optical lattice. The ^{87}Sr $^1S_0-{}^3P_0$ clock transition is subsequently interrogated with laser light propagating collinear with the lattice axis. The geometry is shown schematically in Fig. 1(a). After the spectroscopic probe has redistributed atomic population between the ground $|g\rangle(^1S_0)$ and excited $|e\rangle(^3P_0)$ clock states, the populations are measured via fluorescence detection on the $^1S_0-{}^1P_1$ transition, heating the sample out of the trap. By repeating many such measurements, data are aggregated while the spectroscopy laser is scanned across the clock transition to acquire a spectrum, the probe pulse time is varied to obtain population dynamics, or the laser frequency is stabilized to the clock transition for clock operation.

Details of the setup are described elsewhere [15,16]; here we summarize the important experimental parameters for reference. The atoms are cooled in a two stage magneto-optical trap (MOT) on the transitions indicated by solid arrows in Fig. 1(b). The first stage uses the strong 30 MHz linewidth $^1S_0-{}^1P_1$ transition at 461 nm. The second stage MOT uses dual-frequency narrow line cooling [17,18] on the $^1S_0(F=9/2)-{}^3P_1(F=9/2,11/2)$ intercombination lines (7 kHz) at 689 nm. The optical lattice beam is overlapped with the second stage MOT and atoms are directly cooled into the lattice. The 1D optical lattice is formed by two counterpropagating laser beams near the Stark cancellation wavelength $\lambda=813.43$ nm, where the differential polarizability of $^1S_0$ and $^3P_0$ clock states is zero [7]. In this experiment, a Gaussian beam tilted at a small angle with respect to gravity is focused to a waist $w_0\simeq 30$ μm ($1/e^2$ radius of intensity) and retroreflected by a spherical mirror with matching curvature.

*sebastian.blatt@colorado.edu
†Permanent address: The Niels Bohr Institute, Universitetsparken 5, 2100 Copenhagen, Denmark.
‡Present address: Time and Frequency Division, National Institute of Standards and Technology, 325 Broadway, Boulder, Colorado 80305, USA.
§Present address: AOSense Inc., 767 N. Mary Ave., Sunnyvale, CA 94085-2909, USA.

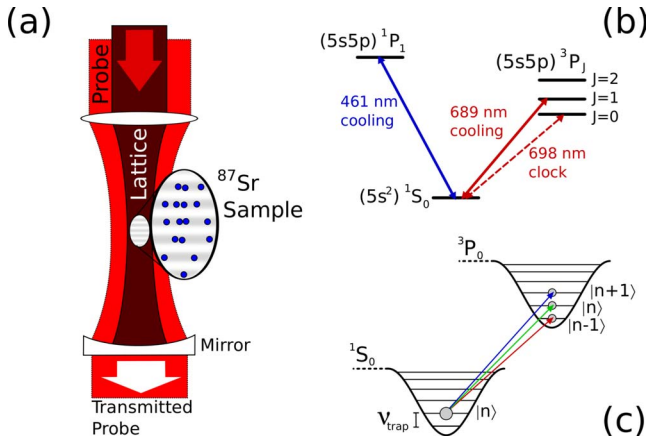

FIG. 1. (Color online) (a) Experimental setup. A one-dimensional optical lattice is oriented vertically along the z axis to suppress tunneling. The lattice wavelength is 813.43 nm. The clock probe beam is aligned collinear with the optical lattice and the probe beam is transmitted by the mirror used to retroreflect the lattice. (b) The optical transitions used to cool are $^1S_0-{}^1P_1$ at 461 nm and $^1S_0-{}^3P_1$ at 689 nm. The spectroscopic transition between the ground $|g\rangle$ and excited $|e\rangle$ clock states is the doubly forbidden intercombination transition $^1S_0-{}^3P_0$ at 698 nm. (c) High quality factor spectroscopy performed on lattice trapped atoms gives rise to three dominant spectral features; a central carrier (green arrow in the middle) where the motional state $|n\rangle$ is conserved accompanied by a red and blue sideband (bottom red and top blue arrows) where the motional state decreases and increases by 1, respectively.

The optical lattice forms in the overlap between the two beams. The typical lattice depth is $U_0 \simeq 130h\nu_{\mathrm{rec}} \simeq 22\ \mu$K, where $\nu_{\mathrm{rec}}=h/(2m\lambda^2)$ is the lattice recoil frequency.

The sample temperature is controlled by additional cooling (heating) resulting in a sample of ~4000 atoms at temperatures variable from 1 to 5 μK. The atoms are Doppler cooled (heated) along the transverse directions and sideband cooling (heating) is performed along the lattice axis with light detuned from the $^1S_0(F=9/2)-{}^3P_1(F=11/2)$ transition.

Using optical pumping, the atoms are then spin-polarized in a weak magnetic field. By choosing the correct polarization for the optical pumping beam, atoms are polarized into one of the two maximally polarized states with magnetic quantum number $m_F=\pm 9/2$. During the polarization step, the sideband cooling (heating) light is simultaneously applied.

For carrier spectroscopy relevant to optical clock operation we probe the $^1S_0-{}^3P_0$ clock transition along the strong confinement axis of the lattice in the Lamb-Dicke regime and the resolved sideband limit [8,9] with a sub-hertz cavity-stabilized diode laser [19]. Here, the trap frequency of 70–80 kHz is much larger than the probe recoil frequency of 4.7 kHz, corresponding to the probe wavelength of 698 nm, and the natural transition linewidth of 1 mHz [20–22]. This ensures a clock interrogation which is highly insensitive to Doppler and recoil effects. The duration of a clock spectroscopy pulse is 80 ms and the probe beam has a ~5 times larger waist than the lattice beam to minimize inhomogeneities introduced by the Gaussian probe beam profile. To probe time-domain Rabi flopping, the pulse time is varied. The motional sidebands are probed with the clock laser detuned by the motional trap frequency.

After applying the spectroscopy pulse, atoms remaining in the ground state are detected by measuring fluorescence on the $^1S_0-{}^1P_1$ transition. This detection pulse heats all $^1S_0$ atoms out of the trap. The population in the $^3P_0$ state is then measured by first pumping the atoms back to the $^1S_0$ state via $^3P_1$ and by again measuring fluorescence on the 461 nm transition. Combining data from these two measurements results in a normalized excitation fraction. The optical lattice is reloaded with a new sample for each new measurement with a ~1 s cycle time.

III. SPECTROSCOPY IN A ONE-DIMENSIONAL OPTICAL LATTICE

Neglecting optical aberrations in the transverse beam profile, the resulting trapping potential near the waist can be written as

$$U(z,r) = -U_0 \cos^2(kz)e^{-2r^2/w_0^2} + mgz, \tag{1}$$

where $r=\sqrt{x^2+y^2}$ designates the transverse distance from the lattice axis, z is the longitudinal coordinate, $k=2\pi/\lambda$ is the lattice wave number, $g \simeq 9.81\ \mathrm{m/s^2}$ is the gravitational acceleration, and m is the mass of ^{87}Sr. The resulting trap is a nearly vertical stack of flat ellipsoids ("pancakes") with an aspect ratio given by lattice wavelength and beam waist.

The gravitational energy shift between neighboring pancakes (~1 kHz) breaks the translational symmetry of the potential and for our trap depths intersite tunneling becomes strongly suppressed [23]. The resulting separation of a lattice band into isolated sites is called a Wannier-Stark ladder [24]. Each site has several states whose energies are determined by the gravity-free lattice structure, but their energy widths decrease according to the residual Landau-Zener tunneling rates to neighboring sites. For our trap depths, temperatures of a few μK, and low site populations, this complex problem simplifies drastically: we can consider single particles in isolated sites, neglect intersite tunneling, and use thermal averaging to evaluate the relevant spectroscopic parameters.

However, even the single site potential is not separable into independent coordinates and it has no analytical solutions. We approximate the longitudinal potential in a site as a one-dimensional harmonic oscillator in z with a quartic distortion. The more gentle transverse confinement given by the Gaussian lattice beam profile is approximated as a two-dimensional harmonic oscillator in r. We also include the first-order coupling term between the longitudinal and transverse degrees of freedom and find

$$U(z,r) \simeq U_0\left(-1 + k^2z^2 + \frac{2}{w_0^2}r^2 - \frac{k^4}{3}z^4 - \frac{2k^2}{w_0^2}z^2r^2\right). \tag{2}$$

Treating the quartic distortion and the coupling term in first-order perturbation theory for harmonic oscillator states $|\boldsymbol{n}\rangle = |n_x,n_y,n_z\rangle$ gives an energy spectrum

$$E_{\boldsymbol{n}}/h \simeq \nu_z\left(n_z+\frac{1}{2}\right)+\nu_r(n_x+n_y+1)-\frac{\nu_{\rm rec}}{2}\left(n_z^2+n_z+\frac{1}{2}\right)$$
$$-\nu_{\rm rec}\frac{\nu_r}{\nu_z}(n_x+n_y+1)\left(n_z+\frac{1}{2}\right), \quad (3)$$

where we identify the longitudinal and transverse trap frequencies from the harmonic approximation to the potential as

$$\nu_z = 2\nu_{\rm rec}\sqrt{\frac{U_0}{h\nu_{\rm rec}}}, \quad (4)$$

$$\nu_r = \sqrt{\frac{U_0}{m\pi^2 w_0^2}}. \quad (5)$$

These relations allow determination of the trap depth and beam waist by measuring the trap frequencies. The number of states in the trap is approximately given by $N_z N_r^2$, with

$$N_z \simeq \frac{U_0}{h\nu_z} = \sqrt{\frac{U_0}{4h\nu_{\rm rec}}}, \quad (6)$$

$$N_r \simeq N_z\frac{\nu_z}{\nu_r}. \quad (7)$$

Typical longitudinal and transverse trap frequencies in our experiment are 80 kHz and 450 Hz, respectively, so that $N_z(N_r)\simeq 6(1000)$. Due to the quartic distortion by the sinusoidal lattice potential, the longitudinal energy gap,

$$\gamma(n_z) \equiv (E_{n_x,n_y,n_z+1}-E_{n_x,n_y,n_z})/h$$
$$=\nu_z-\nu_{\rm rec}(n_z+1)-\nu_{\rm rec}\frac{\nu_r}{\nu_z}(n_x+n_y+1), \quad (8)$$

determines the measured longitudinal trap frequency as approximately $\nu_z-\nu_{\rm rec}$ instead of ν_z. In contrast, the r^2z^2 coupling term in Eq. (2) has a more subtle effect. Radially oscillating atoms explore trap regions with different longitudinal trap frequencies and their response to the spectroscopy laser changes.

Vibrational laser spectroscopy of trapped atoms is a well described topic [8,9]. The Rabi frequency associated with a traveling wave probe of wave vector $\boldsymbol{k}_p$ between initial and final trap states $|\boldsymbol{n}_i\rangle$ and $|\boldsymbol{n}_f\rangle$ is

$$\Omega_{\boldsymbol{n}_f\leftarrow\boldsymbol{n}_i} = \Omega_0\langle\boldsymbol{n}_f|e^{i\boldsymbol{k}_p\cdot\boldsymbol{x}}|\boldsymbol{n}_i\rangle, \quad (9)$$

where the free-space Rabi frequency Ω_0 is given by the dipole matrix element between the electronic states. Thus, atoms in different motional states will respond differently to the same probe field. The resulting spread in Rabi frequencies leads to inhomogeneities in the system for any nonzero temperature.

In the following sections, we will model the most prominent spectroscopic features in a scan across the carrier and motional sideband resonances and compare these models to experimental data to extract information about sample temperatures. The temperature as well as an effective probe laser misalignment will then be used to quantify the degree of inhomogeneity in the system leading to a model of collisional frequency shifts for ultracold fermions in a 1D optical lattice.

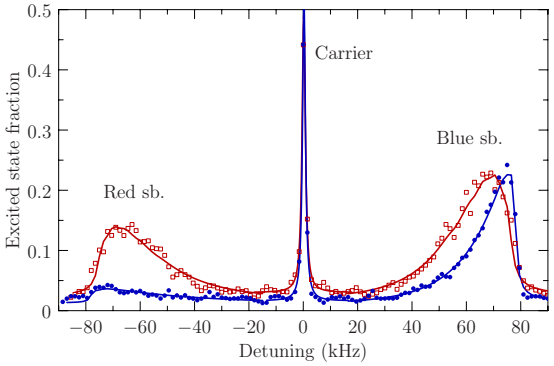

FIG. 2. (Color online) Sideband spectra with longitudinal and transverse cooling (circles) and without in-trap cooling (open squares) by scanning the spectroscopy laser across the electronic transition with a Rabi pulse time of 80 ms and Rabi frequencies on the order of 1 kHz. The solid lines are combinations of fits to the carrier and sidebands.

IV. SIDEBAND SPECTROSCOPY

The motional sideband spectrum of lattice-trapped atoms exhibits features similar to the well known spectra of harmonically trapped ions [9]. Each data point in Fig. 2 was obtained by measuring the excited state fraction after choosing a probe laser detuning in the vicinity of the clock transition and applying an 80 ms Rabi pulse. The traces show a narrow carrier transition that is (mostly) free of motional effects accompanied by motional sidebands at the longitudinal trap frequency ($\nu_z\simeq 80$ kHz). The red-detuned sideband ($n_z\rightarrow n_z-1$) is suppressed with respect to the blue-detuned sideband ($n_z\rightarrow n_z+1$) indicative of the temperature along the strong confinement axis. In contrast to ion trap experiments, the sidebands are smeared out toward the carrier [25]. This skewing is due to the coupling between the longitudinal and transverse degrees of freedom, which makes the longitudinal transition frequency depend on the transverse motional state. The resulting line shape carries information about the potential and the longitudinal and transverse temperatures of the trapped atoms.

The clock transition's natural linewidth is on the order of mHz corresponding to a metastable lifetime on the order of 150 s [20]. At large probe powers, saturation broadening can increase the carrier linewidth to ~1 kHz. At typical Rabi probe times of 80 ms, the population dynamics has dephased to an equilibrium (see Sec. V) allowing a time-independent model of the sideband shape. In the following, we will focus on the first blue longitudinal sideband.

The blue longitudinal sideband is produced by atoms undergoing the clock transition along with a motional transition $|\boldsymbol{n}_i\rangle=|n_x,n_y,n_z\rangle\rightarrow|\boldsymbol{n}_f\rangle=|n_x,n_y,n_z+1\rangle$. The probe laser detuning δ exciting this transition is given by the energy difference in Eq. (8) and depends on the transverse motional state. The relative blue sideband amplitude for a given probe detuning

is thus given by the transverse motional distribution. By assuming a thermal distribution among the transverse trap states, we can relate the shape of the shallow sideband edge (facing the carrier) to the transverse temperature, as shown in the Appendix. We find an approximate line shape as a function of detuning δ from the carrier (valid for the shallow sideband edge):

$$\sigma_{\text{blue}}^{n_z}(\delta) = \frac{\alpha^2}{\tilde{\gamma}(n_z)}\left[1 - \frac{\delta}{\tilde{\gamma}(n_z)}\right] e^{-\alpha[1-\delta/\tilde{\gamma}(n_z)]}\Theta[\tilde{\gamma}(n_z) - \delta], \quad (10)$$

with $\alpha = [\tilde{\gamma}(n_z)/\nu_{\text{rec}}](h\nu_z/k_B T_r)$, uncoupled longitudinal energy gap $\tilde{\gamma}(n_z) = \nu_z - \nu_{\text{rec}}(n_z+1)$, and the Heaviside function Θ. The sideband shape in Eq. (10) is approximately area normalized and its main feature is an exponential slope falling toward the carrier produced by the changing longitudinal energy gap with transverse excursion [the third term in Eq. (8)]. This exponential is multiplied by a linear term rising toward the carrier and vanishing at $\delta = \tilde{\gamma}(n_z)$, which arises from the degenerate two-dimensional transverse confinement. These two features dominate the shape of the sideband and capture the shallow slope toward the carrier. Equation (10) neglects the transition between the shallow edge and the underlying power-broadened Lorentzian that determines the sharp edge.

The final, thermally averaged, blue-detuned sideband absorption cross section is then given by (see the Appendix)

$$\sigma_{\text{blue}}(\delta) \propto \sum_{n_z=0}^{N_z} e^{-E_{n_z}/k_B T_z} \sigma_{\text{blue}}^{n_z}(\delta), \quad (11)$$

as a Boltzmann-weighted superposition of single (longitudinal) state sidebands shifted by the anharmonicity of the longitudinal trap. Here E_{n_z} is the energy of longitudinal state n_z neglecting the $r^2 z^2$ coupling term. In addition, each $n_z \to n_z + 1$ sideband is smeared out toward the carrier by the coupling term between the longitudinal and transverse traps. Each component's base Lorentzian would additionally be broadened by the lifetime of the corresponding Wannier-Stark state. However, for the relevant states and trap depths, this broadening is much smaller than the power-broadened width and can be ignored.

Regardless of the details of the component line shapes in Eq. (11), the only difference between the red and blue sidebands should be that the Boltzmann weights are shifted according to $n_z \mapsto n_z + 1$ since the particle starts in the higher-lying motional state. There is no contribution from the longitudinal ground state to the red sideband cross section and the ratio of integrated sideband absorption cross sections obeys

$$\frac{\sigma_{\text{red}}^{\text{total}}}{\sigma_{\text{blue}}^{\text{total}}} = \frac{\sum_{n_z=1}^{N_z} e^{-E_{n_z}/k_B T_z}}{\sum_{n_z=0}^{N_z} e^{-E_{n_z}/k_B T_z}} = 1 - \frac{e^{-E_0/k_B T_z}}{\sum_{n_z=0}^{N_z} e^{-E_{n_z}/k_B T_z}}, \quad (12)$$

which can be solved numerically for T_z after determining ν_z from the sharp sideband edge on the far side of the carrier, resulting in a line-shape-independent measure of the longitudinal temperature.

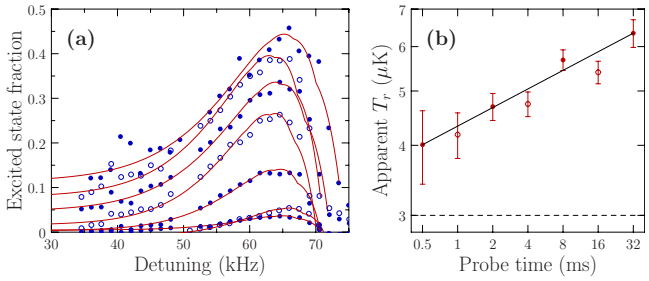

FIG. 3. (Color online) (a) Blue sideband as a function of probe time. The solid curves are fits of Eq. (11) to the data for fixed $T_z = 3$ μK determined from the cross-section ratio in Eq. (12). (b) Apparent transverse temperature as determined from the fits in (a) as a function of probe time on a double-logarithmic plot. The apparent transverse temperature increases with probe time (see text). On the other hand, TOF data indicates constant $T_r = T_z$ (dashed line). The solid line connects the first and last point giving an increase in apparent transverse temperature as ~ 1.5 μK per decade of probe time.

Ideally, the transverse temperature T_r would be determined with the same method by measuring the transverse sidebands at $\delta = \nu_r$, but their amplitude is suppressed since the probe is carefully aligned with the lattice axis. The transverse sidebands can be measured by misaligning the probe beam. An independent measurement of the trap frequency can be obtained by parametric heating. Both methods confirm a typical transverse trap frequency of $\nu_r \simeq 450$ Hz. A combination of a longitudinal sideband spectrum with a transverse trap frequency measurement allows a complete characterization of the trap parameters including depth U_0 and waist w_0 via Eq. (4). This calibration, together with a fit of the longitudinal sideband shape with Eq. (11), then lets us extract information about T_r from the same data that gives ν_z and T_z.

Spectroscopic line shapes of the blue sideband are displayed in Fig. 3(a), along with fits of Eq. (11), for varying Rabi pulse time in the range of 0.5–32 ms. The longitudinal temperature was determined by the ratio of red and blue sideband areas [Eq. (12)] as $T_z = 3$ μK and time-of-flight (TOF) pictures show a unity aspect ratio indicating a well thermalized sample with $T_z = T_r$. Figure 3(b) shows the transverse temperature resulting from the fits in (a) and the dashed line indicates T_z; the solid line connects the first and last points.

The data show an apparent increase in transverse temperature with increasing probe time. A similar measurement with constant pulse time and varying probe power shows no such dependence. In combination with the TOF measurements, we conclude that the transverse temperature is not influenced by the probe laser and that the magnitude of the Rabi frequency does not influence the sideband shape except by broadening the underlying Lorentzian. The time-dependent data suggest that atoms with a broader range of velocities interact with the probe laser than suggested by the steady-state eigenenergy picture that gives rise to Eq. (10). With probe pulse times on the order of the inverse trap frequency, a snapshot of the

atomic distribution can be obtained and the sideband shapes derived above become more applicable.

V. EFFECT OF RADIAL MOTION ON THE CARRIER TRANSITION

The longitudinal sideband shape is strongly modified by the anharmonic corrections to the potential. In contrast we expect the carrier to be insensitive to motional effects since carrier spectroscopy can be done at linewidths of ~2 Hz, corresponding to spectroscopic quality factors of 2×10^{14} [6], which is well in the resolved sideband regime.

The carrier Rabi frequency for a harmonically trapped particle in state $|\boldsymbol{n}\rangle$ probed with a spectroscopy beam of wave vector $\boldsymbol{k}_p=2\pi/\lambda_p\hat{\boldsymbol{k}}_p$ for probe wavelength λ_p is given by

$$\Omega_{\boldsymbol{n}}=\Omega_0\langle\boldsymbol{n}|e^{i\boldsymbol{k}_p\cdot\boldsymbol{x}}|\boldsymbol{n}\rangle=\Omega_0\prod_{i=x,y,z}e^{-\eta_i^2/2}L_{n_i}(\eta_i^2), \tag{13}$$

determined by the Lamb-Dicke parameters $\eta_i\equiv k_p^i a_i/\sqrt{2}$, with oscillator length $2\pi a_i=\sqrt{h/(m\nu_i)}$ for trap axis i and Laguerre polynomial L_{n_i}. In this way, the Rabi frequency is determined by the spatial extent of the motional wave function with respect to the probe wavelength. For a probe that is perfectly aligned with the lattice axis, the only nonzero Lamb-Dicke parameter will be η_z. In this case, $\eta_z^2=\nu_{\mathrm{rec}}^p/\nu_z$, where $\nu_{\mathrm{rec}}^p\simeq4.7$ kHz is the probe recoil frequency.

We ignore corrections to Eq. (13) from perturbed harmonic oscillator states, since both the z^4 and r^2z^2 terms in Eq. (2) produce wave function coefficients suppressed by $\nu_{\mathrm{rec}}/(2\nu_z)$. Although the r^2z^2 coupling modifies η_z, the correction to its value scales as $n_r\sqrt{\nu_{\mathrm{rec}}\nu_r}/\nu_z$ and is negligible for the relevant temperatures. In the following, we will assume harmonic oscillator states and energies and derive carrier line shapes and Rabi flopping accordingly.

Although we can ignore the trap shape except for the harmonic confinement, the Rabi frequency expression still assumes that the particle is probed by a plane wave without transverse profile. Each wave-vector component of the probe beam contributes to the Rabi frequency according to its Fourier coefficient allowing us to estimate the effect of a shaped probe beam. Over the extent of a trap site the probe beam shape can be approximated as a plane wave along the mean probe direction with a transverse shape function describing its intensity profile. Although the probe beam is carefully aligned with the lattice axis, residual misalignment or aberrations might produce a net mismatch between lattice axis $\boldsymbol{k}=k\hat{\boldsymbol{z}}$ and probe axis. Since the transverse trap is isotropic, we choose a small net misalignment angle $\Delta\theta$ along $\hat{\boldsymbol{x}}$, such that $\boldsymbol{k}_p\simeq k_p(\hat{\boldsymbol{z}}+\Delta\theta\hat{\boldsymbol{x}})$. The transverse extent of the probe beam is large and can be approximated by a cylindrically symmetric function (with respect to the net probe direction) of waist $w_p\gg w_0$. The corresponding Rabi frequency is

$$\begin{aligned}\Omega_{n_x,n_z}&=\Omega_0\langle\boldsymbol{n}|e^{i\boldsymbol{k}_p\cdot\boldsymbol{x}}[1+O(a_x^2/w_p^2)]|\boldsymbol{n}\rangle\\&\simeq\Omega_0\langle\boldsymbol{n}|e^{i\boldsymbol{k}_p\cdot\boldsymbol{x}}|\boldsymbol{n}\rangle\\&=\Omega_0e^{-\eta_x^2/2}e^{-\eta_z^2/2}L_{n_x}(\eta_x^2)L_{n_z}(\eta_z^2).\end{aligned} \tag{14}$$

Thus, the transverse shape of a cylindrically symmetric probe beam with large cross section cannot influence the spectroscopy ($a_x^2/w_p^2\simeq10^{-4}$ for our experiment). The Lamb-Dicke parameters are

$$\eta_z=1/\lambda_p\sqrt{h/(2m\nu_z)}, \tag{15}$$

$$\eta_x=\Delta\theta/\lambda_p\sqrt{h/(2m\nu_r)}. \tag{16}$$

Since $\nu_r\ll\nu_z$, even a small amount of effective misalignment will cause significant transverse contributions to the carrier line shape. For our trap frequencies, $\eta_z\simeq0.24$, and $\eta_x\simeq\Delta\theta\times3.2$. In conclusion, the main correction to the carrier Rabi frequency comes from an effective misalignment angle in the transverse direction, while the broad transverse profile can be ignored. This misalignment introduces information about the transverse motional state distribution and thus the transverse temperature into the carrier line shape. We will present experimental evidence for a typical effective misalignment angle $\Delta\theta\simeq10$ mrad.

The carrier line shape for Rabi spectroscopy can be understood as follows. We can neglect spontaneous emission and probe laser decoherence even at Rabi spectroscopy times approaching 1 s [6]. The lattice lifetime has also been measured as ≃1 s and does not introduce decoherence on the typical Rabi pulse times of 80 ms. In this regime, we can neglect any decoherence rates in the system and describe the population dynamics in a fully coherent way. The excited state probability for motional state $|\boldsymbol{n}\rangle$, detuning δ, and pulse time t is

$$p_e(\boldsymbol{n},\delta,t)=\frac{\Omega_{n_x,n_z}^2}{\Omega_{n_x,n_z}^2+\delta^2}\sin^2[\pi t\sqrt{\Omega_{n_x,n_z}^2+\delta^2}]. \tag{17}$$

The ensemble-averaged excited state population is then given by

$$P_e(\delta,t)=\sum_{n_x,n_z}q_{n_x}(T_r)q_{n_z}(T_z)p_e(\boldsymbol{n},\delta,t) \tag{18}$$

for normalized Boltzmann weights q_{n_x} (q_{n_z}) corresponding to transverse (longitudinal) temperature T_r (T_z):

$$q_{n_x}=(1-z_x)z_x^{n_x},\quad z_x\equiv\exp[-h\nu_r/(k_BT_r)], \tag{19}$$

$$q_{n_z}=(1-z_z)z_z^{n_z},\quad z_z\equiv\exp[-h\nu_z/(k_BT_z)]. \tag{20}$$

We are interested in two scenarios: (a) Change the pulse time t and measure Rabi flopping at zero detuning. (b) Change detuning δ by scanning the spectroscopy laser across the carrier resonance and measure the Rabi line shape. Both cases are covered by Eq. (18) and we expect a response as a coherent superposition of slightly different Rabi frequencies.

For low temperatures, we only have to consider atoms in the lowest longitudinal state $n_z=0$ and for small misalignments, the Rabi frequency can be expanded in η_x^2. These two simplifications allow finding an analytical expression for case (a). Here, the excited state population can be approximated as

$$P_e(t) \simeq \sum_{n_x=0}^{\infty} (1-z_x) z_x^{n_x} \sin^2[\phi(1-\eta_x^2 n_x)/2]$$

$$= \frac{1}{2} + \frac{1-z_x}{2} \frac{z_x \cos[\phi(1-\eta_x^2)] - \cos\phi}{1+z_x^2 - 2z_x \cos(\phi\eta_x^2)}, \quad (21)$$

with $\phi = 2\pi t \Omega_0 e^{-\eta_x^2/2} e^{-\eta_z^2/2}$. Equation (21) reduces to $P_e(t) = \sin^2 \phi/2$ for zero misalignment and exhibits dephasing to 1/2 by introducing different frequency components via $\eta_x^2(\Delta\theta)$ and amplifying their contribution by increasing $z_x(T_r)$. For case (b), the sum can be evaluated in a similar manner. The resulting expression does not provide much further insight and we omit it here.

Experimentally, the excited state fraction is obtained by measuring the number of atoms left in the ground state after the spectroscopy pulse, then repumping the excited atoms back to the ground state and measuring their number. The repumping back to the ground state has efficiency $\beta \leq 1$ and can vary from day to day. To obtain an excited state probability independent of a fluctuating overall number of atoms, the fraction of excited state over excited plus ground state counts is used. This normalization results in a Rabi flopping trace that dephases to $\beta/(\beta+1)$ instead of 1/2. Note that on the experimental time scale, the dephasing is a coherent process dominated by an inhomogeneous distribution of Rabi frequencies via effective probe misalignment and temperature.

We investigated the effect of inhomogeneous excitation by mapping out the Rabi flopping and line shapes under different experimental conditions such as sample temperature, misalignment angle, and probe laser intensity. In Fig. 4(a) we show data for the excited state fraction as a function of probe pulse time for two different temperatures. For the hot sample, Rabi oscillations quickly decay after only two to three cycles. For the cold sample, the Rabi oscillations have a significantly higher visibility and are observable for about ten cycles. This behavior was reproduced for a wide range of probe laser intensities. In Fig. 4(b), the Rabi oscillations dephase faster when the effective misalignment angle $\Delta\theta$ is increased by misaligning the probe with respect to the lattice axis. From fits of Eq. (21) we determine a misalignment angle of $\Delta\theta = 10$ mrad for the well-aligned case relevant to clock operation.

Each data point in Fig. 4 is determined by setting a specific probe pulse time and then scanning the probe laser detuning across the carrier transition to obtain a spectrum such as the one shown in Fig. 5 for a probe time of 1.7 ms. The maximum excited state fraction at zero laser detuning ($\sim$0.65 here) would then give the corresponding data point in Fig. 4 for the respective probe time.

For small $\Delta\theta$, the data shown in Figs. 4 and 5 are well reproduced by the simplified model in Eq. (21). This model allows us to determine the transverse temperature as 1 μK for the cooled case, and 3 μK for the uncooled case, with a precision of about 0.2 μK, agreeing well with the corresponding longitudinal temperatures. In the misalignment model, both angle and transverse temperature produce a similar effect so that their covariance is significant. The transverse temperature data have been confirmed by the unity aspect ratio of the atomic cloud in time-of-flight expansion. Accurate determination of the effective misalignment is difficult, introducing larger uncertainty in the radial temperature measurement. However, fitting both Rabi flopping at zero detuning and Rabi line shapes across a wide range of parameters gives consistent results.

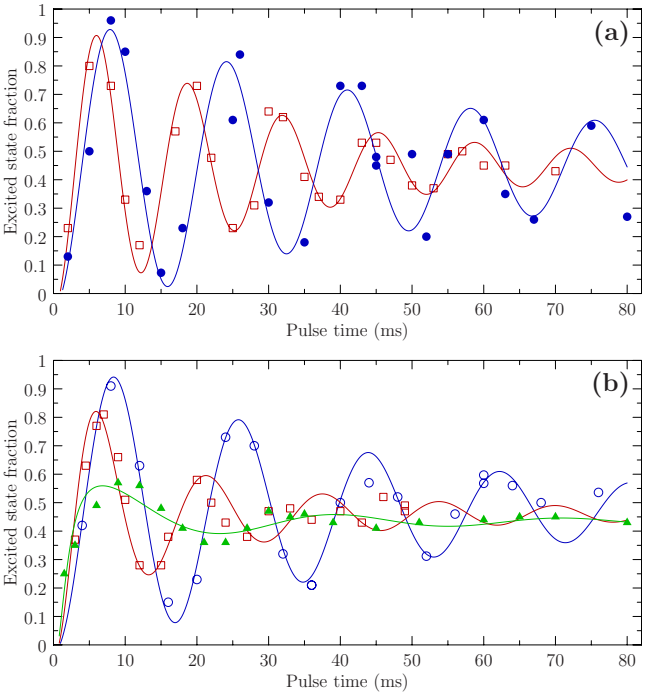

FIG. 4. (Color online) Effect of inhomogeneity on Rabi oscillations. (a) The excited state fraction as a function of pulse time is shown for sample temperatures of 1 μK (circles) and 3 μK (open squares) with fits of Eq. (21), giving bare Rabi frequencies $\Omega_0 = 59$ Hz and 76 Hz, respectively. Both fits result in a misalignment angle $\Delta\theta \simeq 10$ mrad. (b) The excited state fraction as a function of pulse time at 3 μK is shown for increased misalignment angles and probe powers. The open circles show oscillations when the probe beam is slightly misaligned. The fit gives $\Omega_0 = 55$ Hz and $\Delta\theta \simeq 10$ mrad. The open squares show data for increased misalignment and the same probe power giving $\Omega_0 = 54$ Hz and $\Delta\theta \simeq 17$ mrad. Note that the small misalignment approximation used to derive Eq. (21) starts to break down, resulting in a worse fit. Finally, the triangles show data for a large misalignment angle taken with increased power. Although the fit looks much worse, the resulting $\Delta\theta \simeq 40$ mrad agrees well with a geometrical estimate based on the experimental procedure for misaligning the beam.

We characterize the amount of inhomogeneity in the system by the ratio of rms spread in Rabi frequency $\Delta\Omega$ over the site's mean Rabi frequency $\bar{\Omega}$ given by

$$\bar{\Omega} = \sum_{n_x,n_z} q(n_x) q(n_z) \Omega_{n_x,n_z}, \quad (22)$$

$$\Delta\Omega^2 = \sum_{n_x,n_z} q(n_x) q(n_z) \Omega_{n_x,n_z}^2 - \bar{\Omega}^2. \quad (23)$$

In Fig. 6 we show how the ratio $\Delta\Omega/\bar{\Omega}$ changes with sample temperature and misalignment angle. For the temperatures

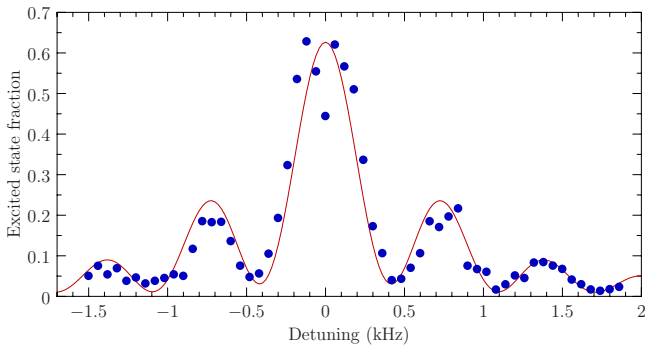

FIG. 5. (Color online) Excitation fraction as a function of probe laser detuning for a probe time of 1.7 ms. The solid curve is a fit of Eq. (18) with the temperature as the only free parameter fixing $\Delta\theta$ at 10 mrad. The fit gives $T_z=T_r=(2.1\pm0.2)$ μK consistent with the sideband method and time-of-flight expansion.

and effective misalignment angles, we find typical values of $\Delta\Omega/\bar{\Omega}$ in the range of 0.05–0.4.

An additional source of Rabi frequency inhomogeneity between different lattice sites is the imperfect transmissivity of the lattice reflector for the probe wavelength introducing a standing wave component in the probe beam. The wavelength mismatch between the lattice and probe beams leads to a modulation of the residual probe standing wave intensity between different lattice sites and, therefore, different Rabi frequencies. However, this effect is different from the excitation induced inhomogeneity discussed above since it is homogeneous within each site. The mirror reflectivity at the probe wavelength was measured as 0.5% leading to a $\Delta\Omega/\bar{\Omega}$ contribution of 0.07. In the following section, we will use the inhomogeneity information obtained from spectroscopy to estimate inhomogeneity-induced clock frequency shifts related to in-site Rabi frequency variation. The Rabi flopping data thus overestimate the in-site Rabi frequency variation slightly.

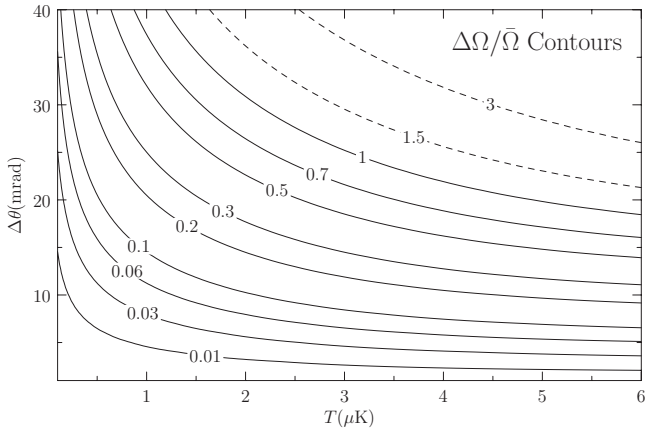

FIG. 6. Contour plot of the relative spread in Rabi frequency $\Delta\Omega/\bar{\Omega}$ as a function of misalignment angle $\Delta\theta$ and temperature $T_z=T_r=T$. The dashed contour lines indicate points where the mean Rabi frequency becomes smaller than the rms spread made possible by the negative values of the Laguerre polynomials in Eq. (14) for large radial quantum numbers. The experimentally relevant range is $\Delta\Omega/\bar{\Omega}=0.05-0.4$.

VI. INHOMOGENEITY-INDUCED DENSITY SHIFTS

For ^{87}Sr at μK temperatures, interatomic collisions are suppressed due to Fermi statistics, which exclude collisions between identical fermions resulting from even partial waves. However, using ^{87}Sr a nonzero density shift to the transition frequency was recently measured [10]. At ultracold temperatures p-wave and higher-order odd partial wave collisions are frozen out and any remaining s-wave interactions should be suppressed. As discussed in the preceding sections, the trapping potential will result in an inhomogeneous excitation process unless all atoms are in the same motional quantum state. Since they are fermions that have been prepared in the same electronic and nuclear states, this is in principle impossible and there will always be an inhomogeneous excitation unless a lattice with at most one particle per site is realized. The inhomogeneous excitation changes the quantum statistics of the trapped atomic sample. This change in statistics leads to distinguishable fermions even for μK temperatures and gives rise to s-wave collisions and therefore a density shift. However, we will show that, under our experimental conditions small density-related frequency shifts can be minimized by choosing an average excitation fraction close to 50%.

The mean-field energy shifts in the two state system consisting of ground and excited clock state $|g\rangle$ and $|e\rangle$ can be expressed as [26]

$$\Delta E_g = \frac{4\pi\hbar^2}{m}(G_{eg}^{(2)}a_{eg}\rho_e + G_{gg}^{(2)}a_{gg}\rho_g), \tag{24}$$

$$\Delta E_e = \frac{4\pi\hbar^2}{m}(G_{ee}^{(2)}a_{ee}\rho_e + G_{eg}^{(2)}a_{eg}\rho_g), \tag{25}$$

where $G_{ij}^{(2)}$ (a_{ij}) is the two-body correlation function (scattering length) between states i and j, and ρ_j is the partial density of state j in a trap site. The above expression is applicable when the de Broglie wavelength of the scattering particles is large compared to their scattering length.

The clock frequency shift can be calculated from the differential energy shift $\Delta E_e-\Delta E_g$. For identical fermions $G_{ii}^{(2)}$ vanishes. Its bosonic equivalent equals 2 and for degenerate bosons it becomes unity. The clock frequency shift $\Delta\nu$ in the two-state fermionic system is given by

$$h\Delta\nu = \frac{4\pi\hbar^2}{m}a_{eg}G_{eg}^{(2)}[\rho_g-\rho_e]. \tag{26}$$

We can estimate the magnitude of this shift by considering the evolution of two representative atoms during the Rabi pulse. These two atoms will follow slightly different trajectories on the Bloch sphere since their Rabi frequencies differ through the inhomogeneities derived in the previous sections causing the energy difference between the clock states to change during the clock pulse.

Under the clock pulse, the electronic state of particle j evolves with the time-dependent Hamiltonian

$$H_j(t) = -\frac{h}{2}\{\Omega_j \sigma_x + [\delta - \Delta\nu(t)]\sigma_z\}, \tag{27}$$

where σ_x (σ_z) is the first (third) Pauli matrix, Ω_j is the Rabi frequency for particle j, and δ is the probe laser detuning from the bare atomic resonance. We assume that all particles are prepared in the excited electronic state $|e\rangle$ and use a discretized version of the Schrödinger equation to propagate the wave function coefficients over a small time step Δt:

$$|\psi_j(t+\Delta t)\rangle = \{I_2 - i\Delta t H_j(t)/\hbar\}|\psi_j(t)\rangle, \tag{28}$$

where I_2 is the 2×2 identity matrix. After each time step Δt, the density shift $\Delta\nu(t)$ is recalculated for the updated wave functions $|\psi_j(t)\rangle \equiv \alpha_j(t)|e\rangle + \beta_j(t)|g\rangle$ $(j=1,2)$ according to Eq. (26). The antisymmetrized two-body correlation function between the two-level fermions 1 and 2 is [10]

$$G_{eg}^{(2)} = 1 - |\alpha_1(t)\alpha_2^*(t) + \beta_1(t)\beta_2^*(t)|^2. \tag{29}$$

A more detailed many-body model relating $G^{(2)}$ to transitions to motional singlet and triplet states in the wave function is presented in Ref. [13].

If we consider a "mean particle" (particle 1) evolving with Rabi frequency $\bar{\Omega}$ and a typical perturbing particle (particle 2) evolving with $\bar{\Omega}+\Delta\Omega$, we can define an approximate associated density shift as

$$\Delta\nu(t) = \Delta\nu_0[1 - |\alpha_1\alpha_2^* + \beta_1\beta_2^*|^2][1 - 2|\alpha_1|^2], \tag{30}$$

where $\Delta\nu_0 \equiv 2\hbar\rho_0 a_{eg}/m$, with average atom density ρ_0. Here, the two-body correlation function is multiplied by the inversion of the mean particle following a trajectory on the Bloch sphere. Due to the background interaction with the other particles, a mean-field energy builds up during the pulse causing the detuning and, thus, the effective Rabi frequency to change dynamically. Many collisions occur during the Rabi time since the rate of collision attempts is given by the inverse of the transverse trap frequency $1/\nu_r \simeq 2$ ms and the typical Rabi time for clock operation is 80 ms. This separation of time scales makes the mean-field treatment applicable. For pulse times $\ll 1/\nu_r$, the above description of the excitation process would have to be modified to include wave packets of vibrational states. For these short pulse times, no collisions can occur which can be explained by a local picture. The atoms are effectively confined to a volume determined by their velocity and the pulse length. If this volume is significantly smaller than the trap size, the local excitation process is very homogeneous. No collisions can occur since the atoms cannot travel far enough to encounter collision partners that have been excited in a slightly different way.

The clock transition frequency is measured by locking the spectroscopy laser to points of equal height on the transition line shape. To model the experimental procedure, we include the mean-field density shift as a time-dependent detuning in the wave function coefficients via Eq. (28). We calculate the line shape for a pulse time corresponding to a π pulse (on resonance for the mean particle) as a function of the inhomogeneity parameter $\Delta\Omega/\bar{\Omega}$ as shown in Fig. 7(a). The measured clock shift can be visualized by comparing two contour

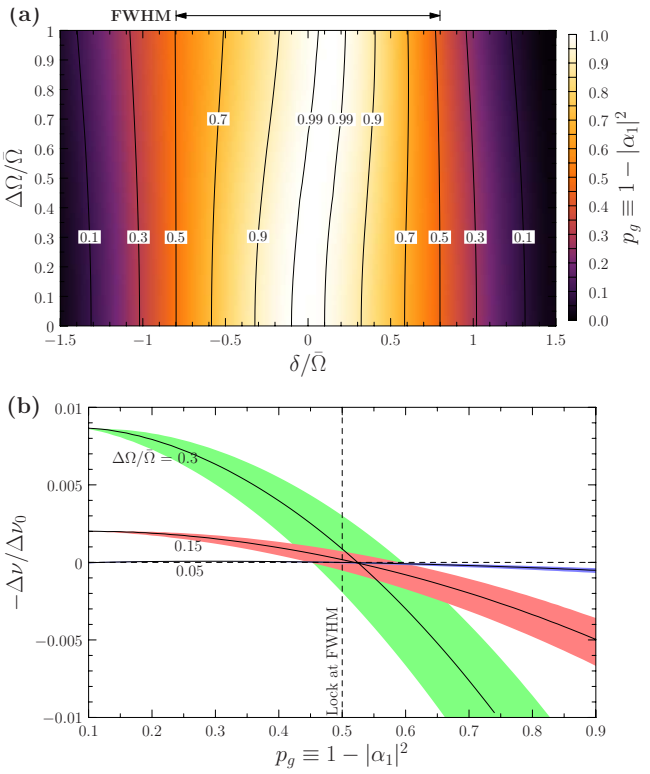

FIG. 7. (Color online) (a) Contour plot of the ground state fraction $p_g = 1 - |\alpha_1|^2$ for the mean particle as a function of detuning in units of $\bar{\Omega}$ and inhomogeneity parameter $\Delta\Omega/\bar{\Omega}$ after a π pulse. The solid curves are contours of equal p_g visualizing the locking points of the spectroscopy laser. Note that the contours for locking close to the full width at half maximum (FWHM) are insensitive to the inhomogeneity parameter. (b) The solid lines show the clock frequency shift (or locking error) with respect to the bare atomic transition in units of $\Delta\nu_0 = 2\hbar a_{eg}\rho_0/m$ as a function of final ground state fraction $p_g = 1 - |\alpha_1|^2$ after the pulse for the relevant range of $\Delta\Omega/\bar{\Omega}$. A negative sign was included in the shift to recreate the experimental behavior for a negative scattering length. The shift crosses zero close to $p_g = 0.5$ and varies quadratically both with inhomogeneity parameter and ground state fraction. The shaded areas indicate the change in the solid curve when the π-pulse condition is allowed to vary by 5%.

lines of equal excited state fraction p_e. The spectroscopy laser is locked to their average detuning which changes with both the inhomogeneity and the pair of contours chosen. The final frequency offset is negative for $p_g < 0.52$, vanishes at $p_g \simeq 0.52$, and becomes positive for $p_g > 0.52$. The resulting frequency shift (or locking error) with respect to the bare atomic transition in units of $\Delta\nu_0$ is shown in Fig. 7(b) for the experimentally relevant range of $\Delta\Omega/\bar{\Omega}$. The frequency shift is shown with a negative sign to recreate the behavior for a negative scattering length a_{eg}.

In using Eq. (29) and detecting only the mean particle excitation fraction, we have chosen a maximally asymmetric model where the representative particle is only perturbed by the background particles but does not act back on the perturbing particles. A maximally symmetric model can be derived by choosing representative Rabi frequencies $\bar{\Omega} \pm \Delta\Omega$

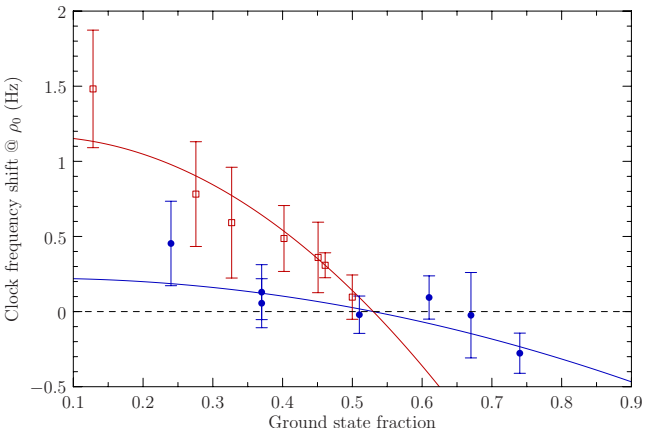

FIG. 8. (Color online) Clock frequency shift for 1 μK (circles) and 3 μK (open squares) normalized to the typical operating density $\rho_0=1\times10^{11}$ cm^{-3}. The solid lines are fits of Eq. (32) to the data with the amplitude as the only fit parameter.

and using the mean of both excited state fractions in Eq. (29) as well as in the detection of the line shape. In this two-particle model, there is no preferred particle and the resulting line shape exhibits loss of contrast as the inhomogeneity grows. We find that the density shift calculated from such line shapes shows a very similar dependence on the ground state fraction and its magnitude is the same.

To extract information about a_{eg} from experimental data for small inhomogeneity, we fit the numerical clock shift data with a simple polynomial. The frequency shift increases quadratically with $\Delta\Omega/\bar{\Omega}$, is quadratic in p_g, and changes sign close to $p_g=0.5$. Fitting the functional form

$$A(p_g-B)(p_g-C)(\Delta\Omega/\bar{\Omega})^2 \tag{31}$$

to numerical data obtained after a π-pulse excitation, as in Fig. 7(b) for $\Delta\Omega/\bar{\Omega}\in[0,0.4]$, results in $A=-0.410(3)$, $B=0.528(1)$, and $C=-0.443(7)$ with rms error 3×10^{-4}. To a good approximation, we can thus use the formula

$$\Delta\nu_\pi \simeq -\Delta\nu_0(\Delta\Omega/\bar{\Omega})^2 0.41(p_g-0.53)(p_g+0.44) \tag{32}$$

to calculate the density shift for small inhomogeneity measured by locking the spectroscopy laser to points of equal ground state fraction after a π pulse (defined on resonance for the mean particle) for particles initially prepared in the excited electronic state. However, if the π-pulse condition is allowed to vary by only 5%, the density shift curve changes as indicated by the shaded areas in Fig. 7(b). Since we cannot exclude such variation over the course of a day, the zero crossing is not well defined and obtains an uncertainty according to how well the probe intensity is stabilized on long time scales. In the following, we will use the standard error given by fitting Eq. (32) to experimental data using weighted least squares to indicate experimental uncertainty and add an estimated relative amplitude error of 30% in quadrature to account for the π-pulse condition uncertainty.

The density shift data from Campbell *et al.* [10] are shown in Fig. 8 along with fits based on Eq. (32) adjusting the amplitude of the polynomial in p_g as the only fit parameter. For temperatures $T_1=1$ μK and $T_2=3$ μK, we find fit amplitudes of $\Delta\nu(T_1)=-2.3\pm0.7$ Hz and $\Delta\nu(T_2)=-12.1\pm0.9$ Hz, respectively. Although we can exclude p-wave scattering contributions [10], the corresponding values of a_{eg} are larger than the unitarity limit given by $a_{eg}=\lambda_T/2\pi$, with thermal wavelength $\lambda_T=h/\sqrt{2\pi m k_B(T+T_{zp})}$ and zero-point temperature $T_{zp}\simeq3.5$ μK corresponding to the ground state energy of the trapping potential. On the other hand, in the unitarity limit, the ratio of both shift coefficients scales as

$$\left[\frac{(\Delta\Omega/\bar{\Omega})_1}{(\Delta\Omega/\bar{\Omega})_2}\right]^2\sqrt{\frac{T_2+T_{zp}}{T_1+T_{zp}}}\simeq0.14, \tag{33}$$

which agrees with the ratio of measured shift coefficients $\Delta\nu(T_1)/\Delta\nu(T_2)=0.2(1)$ for $(\Delta\Omega/\bar{\Omega})_1=0.05$ and $(\Delta\Omega/\bar{\Omega})_2=0.14$ at $\Delta\theta=10$ mrad.

The current two-particle model describes the qualitative behavior of the experimental data well and the scaling factors derived agree with the unitarity limit, but cannot explain the large density shift quantitatively. This discrepancy probably stems from applying Eq. (26) in a dynamic context. Even though there are many collisions during a typical Rabi pulse time, Eq. (26) describes the mean-field differential energy shift in a two-level system in steady state and cannot model the line shape evolution during the Rabi pulse accurately. A full many-body model is expected to improve our understanding of the density shift considerably [13]. Even with a better model, extracting reliable information about the scattering lengths from density shift data remains a challenging problem.

VII. CONCLUSION

In this paper we have investigated the inhomogeneous excitation introduced by the transverse degrees of freedom for Rabi spectroscopy in a 1D optical lattice. An analytical model for how the longitudinal sidebands are influenced by the finite temperature of the atomic sample is developed and is used to allow us to extract temperatures from sideband scans. Furthermore, by modeling and fitting Rabi oscillations and line shapes the degree of inhomogeneity introduced by transverse temperature and an effective probe beam misalignment can be measured. The inhomogeneity directly affects the spectroscopic process and causes otherwise identical ultracold fermions to become distinguishable during the excitation process. This effect is modeled by a time-dependent two-particle correlation function, giving rise to density-dependent clock frequency shifts. By determining the temperature and inhomogeneity of the atomic sample as described here and by controlling the excitation fraction, this density shift can now be measured, controlled, and zeroed. We have presented a simple two-particle model that models the density shift data qualitatively.

ACKNOWLEDGMENTS

We acknowledge early contributions by T. Zelevinsky to the discussion on probe inhomogeneities and technical con-

tributions by T. L. Nicholson and M. H. G. de Miranda. We thank A. M. Rey and K. Gibble for insightful discussions. This work was supported by funding from NIST, NSF, DARPA, and ONR.

APPENDIX: SIDEBAND LINE-SHAPE DERIVATION

The derivation in this appendix generalizes arguments presented by Boyd [15], Le Targat [27], and Ludlow [16] to include longitudinal anharmonicity and population in higher bands. An atom's radial motional state (n_x,n_y) shifts the sideband transition frequency via the r^2z^2 coupling term in the site potential. For a fixed longitudinal quantum number n_z and detuning δ, only atoms with specific longitudinal quantum numbers (n_x,n_y) will be resonant with the probe laser. This resonance condition is given by the longitudinal energy gap γ [Eq. (8)]. The sideband amplitude at this detuning is determined by the Boltzmann factors for the corresponding quantum numbers. The single-n_z sideband line shape is a superposition of individual atomic transitions between states $|i\rangle=|n_x,n_y\rangle$ and $|f\rangle=|n_x,n_y,n_z+1\rangle$ weighted by the Boltzmann distribution. The individual atomic transition is power broadened with base width Γ, given by the carrier Rabi frequency, since the natural transition linewidth is negligible. We also neglect higher-order contributions to the sideband where the change in longitudinal quantum number is accompanied by a change in the radial quantum numbers since their amplitude is suppressed by an additional factor of η_x^2. We find

$$\sigma_{\mathrm{blue}}^{n_z}(\delta) \propto \sum_{n_x,n_y} \frac{z_r^{n_x} z_r^{n_y}}{1+\frac{4}{\Gamma^2}[\delta-\gamma(n_z)]^2}, \tag{A1}$$

where $z_r=\exp[-h\nu_r/(k_B T_r)]$ is the Boltzmann factor associated with transverse state n_x (n_y) and transverse temperature T_r. By introducing a radial quantum number $n_r \equiv n_x+n_y$ and corresponding two-dimensional degeneracy factor (n_r+1), we can reduce the summation to one dimension:

$$\sigma_{\mathrm{blue}}^{n_z}(\delta) \propto \sum_{n_r} \frac{(n_r+1) z_r^{n_r+1}}{1+\frac{4}{\Gamma^2}\left[\delta-\tilde{\gamma}(n_z)+\nu_{\mathrm{rec}}\frac{\nu_r}{\nu_z}(n_r+1)\right]^2}, \tag{A2}$$

with base longitudinal gap $\tilde{\gamma}(n_z) \equiv \nu_z - \nu_{\mathrm{rec}}(n_z+1)$.

For detunings $\delta/\tilde{\gamma}(n_z) \ll 1$ on the shallow sideband slope facing the carrier, the sum's main term will be associated with the quantum number n_r that minimizes the denominator leading to a relation between detuning and quantum number:

$$n_r+1 \simeq -\frac{\nu_z}{\nu_{\mathrm{rec}}\nu_r}[\delta-\tilde{\gamma}(n_z)]. \tag{A3}$$

We approximate the sum by this main term and find

$$\sigma_{\mathrm{blue}}^{n_z}(\delta) \propto \left[1-\frac{\delta}{\tilde{\gamma}(n_z)}\right] e^{-\alpha[1-\delta/\tilde{\gamma}(n_z)]}\Theta[\tilde{\gamma}(n_z)-\delta], \tag{A4}$$

with $\alpha \equiv [\tilde{\gamma}(n_z)/\nu_{\mathrm{rec}}](h\nu_z/k_B T_r)$. We ensure the applicability of the approximation by cutting off the line shape at $\delta=\tilde{\gamma}(n_z)$ with the Heaviside function Θ. For the relevant parameter ranges, the line shape can be approximately area normalized to three significant figures with a prefactor $\alpha^2/\tilde{\gamma}(n_z)$.

The longitudinal trap anharmonicity places each of these single-band component line shapes at slightly different detunings. We find the final blue sideband line shape as a Boltzmann-weighted superposition of area-normalized components:

$$\sigma_{\mathrm{blue}}(\delta) = \left(\sum_{n_z}^{N_z} e^{-E_{n_z}/k_B T_z}\right)^{-1} \sum_{n_z}^{N_z} e^{-E_{n_z}/k_B T_z} \sigma_{\mathrm{blue}}^{n_z}(\delta),$$

$$E_{n_z}/h = \nu_z\left(n_z+\frac{1}{2}\right) - \frac{\nu_{\mathrm{rec}}}{2}(n_z^2+n_z+1). \tag{A5}$$

Here, the quartic approximation to the longitudinal potential reproduces the lowest energies and gaps to within a few percent. A better approximation to the energy E_n of the nth longitudinal state is given by $E_n/(h\nu_{\mathrm{rec}})=[a_n(q)+b_{n+1}(q)]/2+2q$, where a_n and b_{n+1} are the characteristic values of the Mathieu equation bounding its nth stability region at parameter value q (see Ref. [28], for example). Here q has to be optimized numerically—starting from the harmonic approximation $q_0=U_0/(4h\nu_{\mathrm{rec}})$—such that the lowest gap $(E_1-E_0)/h \simeq \nu_{\mathrm{rec}}[a_1(q)-a_0(q)]$ is equal to the measured longitudinal trap frequency.

[1] A. D. Ludlow *et al.*, Science **319**, 1805 (2008).
[2] G. K. Campbell *et al.*, Metrologia **45**, 539 (2008).
[3] T. P. Heavner, S. R. Jefferts, E. A. Donley, J. H. Shirley, and T. E. Parker, Metrologia **42**, 411 (2005).
[4] S. Bize *et al.*, J. Phys. B **38**, S449 (2005).
[5] S. Weyers, U. Hübner, R. Schröder, C. Tamm, and A. Bauch, Metrologia **38**, 343 (2001).
[6] M. M. Boyd, T. Zelevinsky, A. D. Ludlow, S. M. Foreman, S. Blatt, T. Ido, and J. Ye, Science **314**, 1430 (2006).
[7] J. Ye, H. J. Kimble, and H. Katori, Science **320**, 1734 (2008).
[8] D. J. Wineland and W. M. Itano, Phys. Rev. A **20**, 1521 (1979).
[9] D. Leibfried, R. Blatt, C. Monroe, and D. Wineland, Rev. Mod. Phys. **75**, 281 (2003).
[10] G. K. Campbell *et al.*, Science **324**, 360 (2009).
[11] X. Baillard *et al.*, Eur. Phys. J. D **48**, 11 (2008).
[12] T. Akatsuka, M. Takamoto, and H. Katori, Nat. Phys. **4**, 954 (2008).
[13] A. M. Rey, A. V. Gorshkov, and C. Rubbo, e-print arXiv:0907.2245.
[14] K. Gibble, Phys. Rev. Lett. **103**, 113202 (2009).
[15] M. M. Boyd, Ph.D. thesis, University of Colorado, 2007

(http://jilawww.colorado.edu/yelabs/pubs/theses.html).
[16] A. D. Ludlow, Ph.D. thesis, University of Colorado, 2008 (http://jilawww.colorado.edu/yelabs/pubs/theses.html).
[17] T. Mukaiyama, H. Katori, T. Ido, Y. Li, and M. Kuwata-Gonokami, Phys. Rev. Lett. **90**, 113002 (2003).
[18] T. H. Loftus, T. Ido, A. D. Ludlow, M. M. Boyd, and J. Ye, Phys. Rev. Lett. **93**, 073003 (2004).
[19] A. D. Ludlow, X. Huang, M. Notcutt, T. Zanon-Willette, S. M. Foreman, M. M. Boyd, S. Blatt, and J. Ye, Opt. Lett. **32**, 641 (2007).
[20] M. M. Boyd, T. Zelevinsky, A. D. Ludlow, S. Blatt, T. Zanon-Willette, S. M. Foreman, and J. Ye, Phys. Rev. A **76**, 022510 (2007).
[21] S. G. Porsev and A. Derevianko, Phys. Rev. A **69**, 042506 (2004).
[22] R. Santra, K. V. Christ, and C. H. Greene, Phys. Rev. A **69**, 042510 (2004).
[23] P. Lemonde and P. Wolf, Phys. Rev. A **72**, 033409 (2005).
[24] M. Glück, A. R. Kolovsky, and H. J. Korsch, Phys. Rep. **366**, 103 (2002).
[25] A. D. Ludlow, M. M. Boyd, T. Zelevinsky, S. M. Foreman, S. Blatt, M. Notcutt, T. Ido, and J. Ye, Phys. Rev. Lett. **96**, 033003 (2006).
[26] D. M. Harber, H. J. Lewandowski, J. M. McGuirk, and E. A. Cornell, Phys. Rev. A **66**, 053616 (2002).
[27] R. Le Targat, Ph.D. thesis, LNE-SYRTE, 2007 (http://tel.archives-ouvertes.fr/tel-00170038).
[28] J. C. Slater, Phys. Rev. **87**, 807 (1952).